Journal of Volcanology and Geothermal Research 313 (2016) 1–14

Contents lists available at ScienceDirect

Journal of Volcanology and Geothermal Research

journal homepage: www.elsevier.com/locate/jvolgeores

Timing and composition of continental volcanism at Harrat Hutaymah, western Saudi Arabia

Robert A. Duncan [a,b,*], Adam J.R. Kent [a], Carl R. Thornber [c], Tyler D. Schlieder [a], Abdullah M. Al-Amri [b]

[a] College of Earth, Ocean, and Atmospheric Sciences, Oregon State University, Corvallis, OR 97333, USA
[b] Department of Geology and Geophysics, King Saud University, Riyadh, Saudi Arabia
[c] U.S. Geological Survey, Cascades Volcano Observatory, Vancouver, WA, USA

ARTICLE INFO

Article history:
Received 16 October 2015
Accepted 15 January 2016
Available online 28 January 2016

Keywords:
Harrats
Age determinations
Continental volcanism
Afar hotspot
Lithosphere–asthenosphere boundary

ABSTRACT

Harrat Hutaymah is an alkali basalt volcanic field in north-central Saudi Arabia, at the eastern margin of a large Neogene continental, intraplate magmatic province. Lava flow, tephra and spatter cone compositions in the field include alkali olivine basalts and basanites. These compositions contrast with the predominantly tholeiitic, fissure-fed basalts found along the eastern margin of the Red Sea. The Hutaymah lava flows were erupted through Proterozoic arc-associated plutonic and meta-sedimentary rocks of the Arabian shield, and commonly contain a range of sub-continental lithospheric xenoliths, although the lavas themselves show little indication of crustal contamination. Previous radiometric dating of this volcanic field (a single published K–Ar age; 1.8 Ma) is suspiciously old given the field measurement of normal magnetic polarity only (i.e. Brunhes interval, ≤780 Ka). We report new age determinations on 14 lava flows by the ^{40}Ar–^{39}Ar laser step heating method, all younger than ~850 Ka, to better constrain the time frame of volcanism, and major, trace and rare earth element compositions to describe the chemical variation of volcanic activity at Harrat Hutaymah. Crystal fractionation was dominated by olivine ± clinopyroxene at a range of upper mantle and crustal pressures. Rapid ascent and eruption of magma is indicated by the array of lower crustal and lithospheric xenoliths observed in lava flows and tephra. Modeling suggests 1–7% melting of an enriched asthenospheric mantle source occurred beneath Harrat Hutaymah under a relatively thick lithospheric cap (60–80 km).

1. Introduction

1.1. The Harrat Province

One of the largest alkali basalt provinces in the world (area: 180,000 km^2) is located in the western part of the Arabian Peninsula (Fig. 1). These extensive Cenozoic basaltic lava fields (in Arabic "harrats") erupted predominantly from N–S oriented volcanic centers that lie within 500 km of the NW-trending eastern margin of the Red Sea. The origin of these fields appears to be related to regional extension and thinning of thick, Arabian–Nubian Pan-African craton that began ~30 Ma (Camp and Roobol, 1992; Coleman, 1993). Curiously, there is no equivalent of this volcanic activity in eastern Egypt and Sudan, on the opposite side of Africa–Arabia plate separation (Bohannon et al., 1989). In contrast with tholeiitic basalts of the Red Sea spreading system, lava compositions in the region of the harrats include alkali olivine basalts, olivine-transitional basalts, and hawaiites, with minor more evolved compositions. Early volcanism (>12 Ma), aligned with the NW orientation of the opening Red Sea, was dominated by tholeiitic to transitional compositions, but since then compositions have become more alkalic, and erupted from younger, more broadly distributed N–S oriented volcanic centers (<12 Ma). A prominent N–S alignment of relatively large volume volcanic fields, the Makkah–Madinah–Nafud (MMN) line, coincides with the Ha'il Arch, a structural axis of uplift of the Arabian shield, beginning ~15 Ma.

1.2. Harrat Hutaymah

Harrat Hutaymah (Fig. 2), one of the smallest and youngest harrats, assembled from monogenetic cones and lava flows covering ~900 km^2, is also the easternmost harrat, ~500 km from the Red Sea axis (Thornber, 1992). Previous work at Hutaymah, which includes geochemical and petrologic studies, and K–Ar age determinations (Pallister, 1984; Thornber, 1992), reveals that Harrat Hutaymah is dominated by a compositionally narrow range of alkaline basalts, from basanite to trachy-basalt, that erupted from 15 main centers. Compared to other Arabian harrats, Hutaymah presents an unusual abundance of explosive volcanism and crust- and mantle-derived xenolithic material, including igneous pyroxenite, melt-bearing peridotite and metamorphic pyroxenite (Thornber, 1992). Previous models for the petrogenesis of Harrat Hutaymah, and the harrat province as a whole, attribute the volcanism to decompression melting of mantle

* Corresponding author at: College of Earth, Ocean, and Atmospheric Sciences, Oregon State University, Corvallis, OR 97333, USA
E-mail address: rduncan@coas.oregonstate.edu (R.A. Duncan).

http://dx.doi.org/10.1016/j.jvolgeores.2016.01.010
0377-0273/

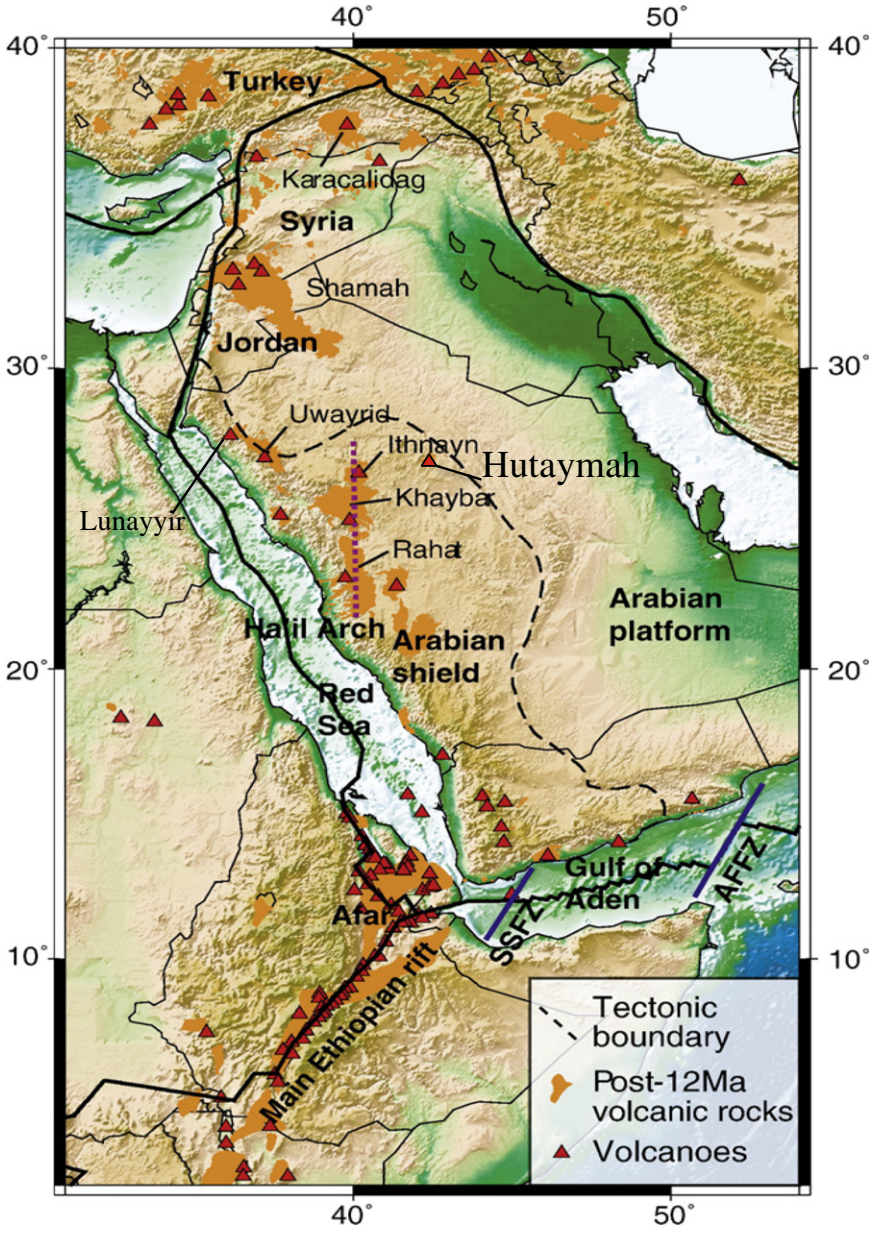

Fig. 1. Location map for volcanic fields ("harrats") in western Saudi Arabia. Individual harrats lie within 500 km of the Red Sea margin, but eruptive centers/fissures are aligned predominantly N–S. The most voluminous fields fall along the axis indicated by dotted red line (Ha'il Arch), also called the Makkah–Medinah–Nafud (MMN) lineament. Harrat Hutaymah is a relatively small field that lies east the MMN line.
After Chang and van der Lee, 2011.

upwelling in response to plate thinning and separation along the eastern flank of the Red Sea Rift (Hempton, 1987; Pallister, 1987; Coleman and McGuire, 1988).

A recent study of Harrat Lunayyir, located west of Harrat Hutaymah, suggests that some previous K–Ar ages reported for many harrats may be inaccurate because of the common occurrence of xenolithic fragments that carry 'excess' (undegassed, non-atmospheric) argon (Duncan and Al-Amri, 2013). Variation in major and trace element compositions of erupted lavas throughout the harrat province appears the reflect differences in depth and degree of melting of either lithospheric mantle or asthenosphere (or both), in response to the tectonic thinning (Camp et al., 1991; Duncan and Al-Amri, 2013). An additional consideration is the possible influence of asthenospheric flow from the Afar plume, which may be channeling warm mantle beneath the Arabian shield (Camp et al., 1991; Chang and Van der Lee, 2011).

The location of Harrat Hutaymah on the eastern edge of the harrat province, the extensive geochemical work produced by Thornber (1992), and the uncertain reported K–Ar ages make Hutaymah an ideal location to add information about the timing and compositions of volcanic activity, with new age determinations using high precision ^{40}Ar–^{39}Ar laser step heating experiments, and further geochemical data. Our new results are compared with previous data from Harrat Lunayyir (Duncan and Al-Amri, 2013), Harrat Rahat (Camp and Roobol, 1992; Moufti et al., 2012), and the Red Sea (e.g. Vlastelic et al., 1998; Kelley et al., 2013) to map the regional trends in lava composition in time and location. We conclude that Hutaymah volcanism is the result of decompression melting of subcontinental lithosphere and asthenosphere (60–80 km depth), in response to regional extension and/or thermal erosion by northward asthenospheric flow from the Afar hot spot.

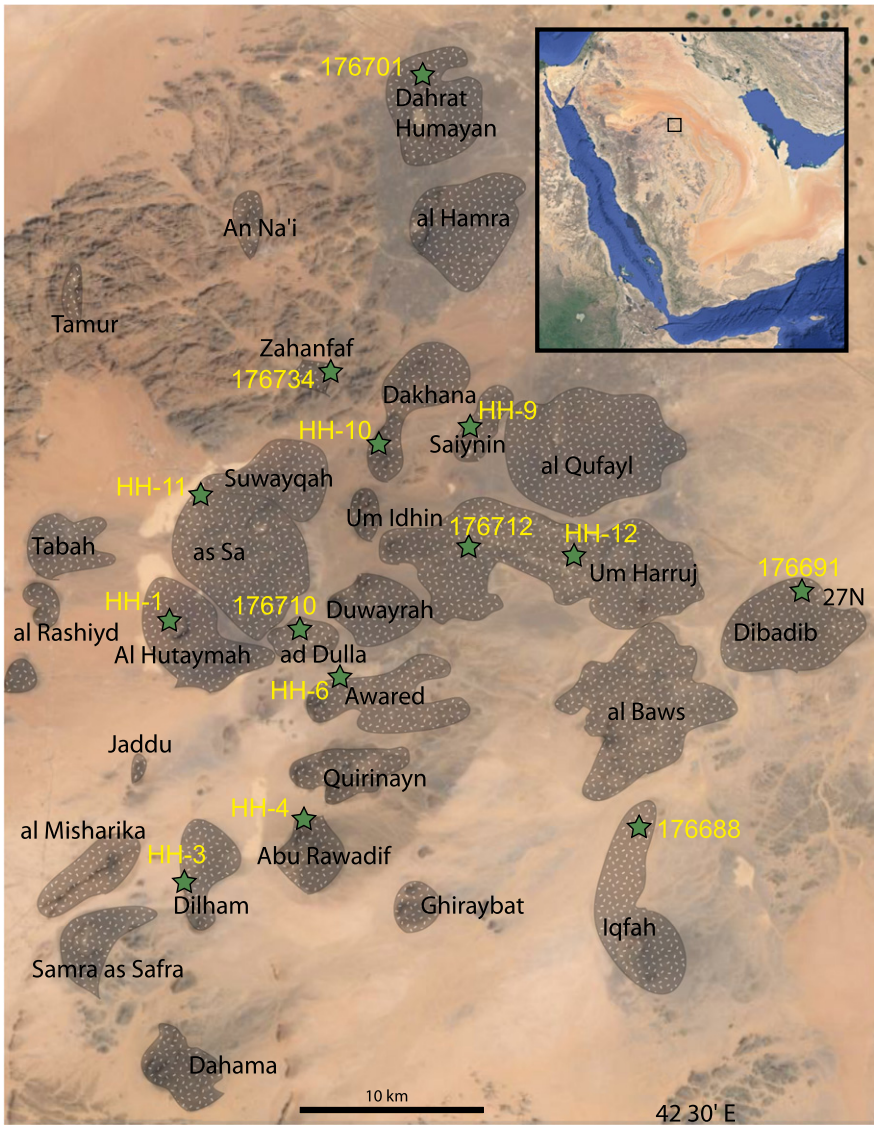

Fig. 2. Harrat Hutaymah, western Saudi Arabia. The various volcanic centers, mapped in detail by Thornber (1990), are indicated as shaded areas on this satellite image. The green stars mark the location of samples collected for age determinations and geochemical analyses.

1.3. Volcanology

Harrat Hutaymah volcanism is restricted to a narrow range of alkaline mafic lava compositions that cover a relatively small area (~900 km^2) compared to other Arabian harrats (Thornber, 1992). The name derives from one of the most prominent volcanic centers in the area, *Al Hutaymah*, a large ~1 km diameter, 300 m deep tuff ring (maar), located in the west central area of the volcanic field (Bramkamp et al., 1963; Thornber, 1992). Al Hutaymah is one of 15 main eruptive centers within this volcanic field. In addition to large craters, the Hutaymah volcanic field presents an unusual abundance of tuff rings (maars), indicating explosive activity resulting from interactions between magma and water, i.e., phreatomagmatic style eruptions (Thornber, 1992).

The concentration of explosive activity at Hutaymah is reflected in the abundant tephra deposits and variable crater morphology (Thornber, 1992). Isolated maars (craters rimmed by tuff rings) can be found at Al Hutaymah, Tabah, Tamur, An Na'i, and Al Hamra. Isolated tuff ring rimmed craters that have been largely in-filled by Quaternary alluvium are found at Samra as Safra, Dibadib, Dahrat Humayan, and Dakhana, and with grouped vents of similar morphology at Jabal Dilham, Jabal Um Harruj, Jabal Duwayrah, as Sa, Jabal Al Qufayl, and Saiynin (Fig. 2). Commonly, reworked tephra can be found radially distributed from the tuff rings, covering an area of 10–60 km^2. Large lava flows up to 60 km^2 and 40 m thick overlie nested tuff rings at Al Jaddu, Al Hamra, and as Sa, and the inverse relationship, tuff-ring tephra superimposed over coherent flows, can be viewed in maar walls at Al Hutaymah and Jabal Iqfah (Thornber, 1992). Approximately 85 small alkali basaltic cinder/spatter cones (<1 km diameter) and fissures (<1–2 km length) produced scoria and small a'a flows (with minor pahoehoe flows) (Thornber, 1992). A defining characteristic of Hutaymah volcanism is the abundance of ultramafic xenoliths and megacrysts distributed throughout the tephra, flows, and spatter cones, likely sourced from the lower crust or upper mantle (Thornber, 1990). Collectively, these isolated and grouped cones, maars, tuff-rings, and elongate fissure eruptions define the eruptive characteristics of the entire harrat (Thornber, 1992).

The vents (spatter cones, tuff rings, fissures) are aligned along a series of northerly to north–northeasterly trending lineaments (Pallister, 1984). Individual vent clusters are also elongated in the north–south direction. According to Pallister (1984) this alignment does not conform with the structural fabric of underlying Proterozoic rocks, but indicates a significant shift in orientation of the Quaternary stress field relative to

the older crustal structures and relative to the NW–SE trend of the Red Sea axis.

2. Methods

We examined fifty-seven lava flow samples from Harrat Hutaymah, including a subset of a collection made by one of us as the basis of a PhD dissertation (5-digit identifiers, Thornber, 1992), and augmented by field work by two of us (HH-identifiers, RAD and AMA) in 2013. We categorized samples in hand sample and thin section, and divided these into groups based on spatial distribution, texture, and mineralogy for dating and geochemical analysis. Samples unsuitable for age determinations based on alteration or xenocrystic inclusions were excluded from further analysis. We selected samples for dating that were aphyric to sparsely phyric, well-crystallized and lacking interstitial glass.

We obtained bulk rock major and minor element concentrations (Table 1) for our samples at the GeoAnalytical Laboratory at Washington State University (WSU) using the X-ray fluorescence (XRF) method (Johnson et al., 1999) and selected samples were analyzed for trace element concentrations (Table 2) by inductively coupled plasma source mass spectrometry (ICP-MS; Knaack et al., 1994). For analysis a dilithium tetraborate flux was mixed with a portion of the rock powder (2:1 ratio for XRF; 1:1 ratio for ICP-MS) to produce fused beads. Based on replicate analyses the estimated uncertainties (at $\pm 2s$) for XRF major element measurements are <1% for all elements. Estimated uncertainties for trace elements ($\pm 2s$) by XRF are <80% for Pb, Th, and U; <40% for Rb, Ce; <25% for Nb, La, Ce and Nd, and <5% for all other elements. For trace elements analyses by ICP-MS estimated uncertainties are <20% for U and Th, <10% for Cs and <5% (2s) for all other elements (Knaack et al., 1994). Further details on precision and detection limits are given in Knaack et al. (1994) and Johnson et al. (1999). We also provide major and trace element data (see Supplementary Geochemical Data) for the older collection of samples. Major element concentrations were determined using electron microprobe analysis of glasses fused from whole rock powders (Thornber, 1992) and trace element concentrations were determined by instrumental neutron activation analysis (INAA) methods (Baedecker and McKown, 1987).

We performed age determinations of groundmass separates at Oregon State University with standard ^{40}Ar–^{39}Ar laser step heating methods. Whole rock samples were crushed, sieved, washed, and subjected to mild acid leaching with HCl and HNO_3 then hand-picked to remove phenocryst phases. Some 100 mg of prepared groundmass of each sample was next irradiated for 6 h in the 1MW TRIGA nuclear reactor at Oregon State University, along with flux monitor FCT sanidine (28.201 Ma; Kuiper et al., 2008). Irradiated samples were loaded into Cu-planchettes in an ultra-high vacuum sample chamber and incrementally heated (in 16-33 steps, from 400 °C to fusion) by scanning a defocused 25W CO_2 laser beam in preset patterns across each sample, in order to release the Ar evenly. Argon isotope compositions of irradiated samples were determined using the Thermo Scientific Model ARGUS VI multi-collector with five fixed Faraday detectors (all fitted with 10^{12} Ω resisters) and 1 ion-counting CuBe electron multiplier, allowing simultaneous measurement of all Ar isotopes, with mass 36 on the ion multiplier and masses 37 through 40 on the four adjacent Faraday cups. Gas cleanup occurred in a small-volume, all-metal extraction line equipped with Zr–Al getters. We monitored the atmospheric correction with an air pipette system, and cross-calibrated the 5 collectors for small differences in sensitivity, on a daily basis. We calculated ages (reported at $\pm 2\sigma$ uncertainty) in several ways (Table 3). Plateau ages are the weighted (by inverse variance) means of concordant, sequential step ages while isochron ages are derived from regressions of the same heating step isotopic compositions. All calculations were performed using the ArArCALC v2.6.2 software package (Koppers, 2002).

We modeled conditions and compositions of parental melt generation and evolution using the MELTS software package (Ghiorso and Sack, 1995). Oxygen fugacity was buffered at the quartz–fayalite–

Table 1
Major and trace element concentrations for basaltic whole rocks, Harrat Hutaymah.

Samples	HH-1	HH-3	HH-4	HH-6	HH-9	HH-10	HH-11	HH-12	176701	176734
Latitude, N	26°58.867	26°50.617	26°56.083	26°57.617	27°06.333	27°04.767	27°04.033	27°02.750	27°07.717	27°04.050
Longitude, E	42°14.400	42°15.017	42°19.283	42°19.483	42°25.283	42°21.650	42°15.867	42°25.500	42°22.300	42°20.950
SiO_2	45.97	45.43	47.05	45.10	47.75	44.97	48.94	44.68	46.08	46.08
TiO_2	2.802	2.272	2.694	2.847	1.721	2.568	1.998	2.547	13.95	15.04
Al_2O_3	15.48	14.85	15.35	15.34	15.00	14.96	15.84	14.58	11.39	10.87
FeO*	12.23	11.36	10.63	11.07	11.05	11.19	11.69	11.94	10.04	10.08
MnO	0.198	0.183	0.166	0.173	0.165	0.185	0.190	0.195	10.28	9.33
MgO	7.09	10.51	7.32	7.65	10.18	8.68	6.99	8.05	3.31	4.42
CaO	8.88	9.90	9.55	9.76	10.02	10.82	9.81	10.48	1.22	1.58
Na_2O	4.58	3.64	4.25	4.23	3.25	2.73	3.56	3.69	2.34	2.58
K_2O	1.56	1.18	1.83	1.70	0.64	1.29	0.69	1.29	0.17	0.14
P_2O_5	0.599	0.490	0.494	0.566	0.227	0.471	0.282	0.524	0.37	0.52
Sum	99.39	99.81	99.33	98.44	100.02	97.85	99.99	97.97	99.18	100.64
Mg#	53.73	64.95	57.96	58.06	64.86	60.84	54.49	57.47	64.38	63.22
Ni	92	272	146	156	209	178	136	142	164	214
Cr	229	317	180	189	480	348	225	381		
Sc	20	23	19	19	23	22	25	24		
V	201	239	199	222	218	242	229	235		
Ba	353	378	543	528	197	380	486	346	295	417
Rb	24	21	27	27	9	19	8	22		
Sr	793	718	904	939	457	958	460	1012	644	849
Zr	226	191	229	227	111	190	119	224	167	181
Y	24	22	21	20	18	23	25	22	25	24
Nb	83.4	72.1	82.5	86.9	29.2	76.6	27.1	87.4	71.0	84.0
Ga	19	19	20	22	19	19	21	19		
Cu	51	85	64	68	82	60	98	58	70	80
Zn	90	91	86	87	91	82	106	96	126	151
Pb	2	2	4	2	1	2	2	2	2	
La	36	44	49	50	15	34	14	35		
Ce	70	70	82	81	31	68	37	74	71	86
Th	5	7	7	9	3	6	3	4		
Nd	34	28	33	31	18	30	18	33		
U	2	2	4	3	1	2	0	2		

Table 2
Chondrite-normalized rare earth element concentrations for whole rocks, Harrat Hutaymah.

Samples	HH-1	HH-3	HH-4	HH-6	HH-9	HH-10	HH-11	HH-12	176701	176734
La	151.73	169.63	200.93	207.06	65.32	150.90	72.68	152.83	144.34	199.75
Ce	119.73	115.57	134.24	137.28	49.72	110.60	54.65	119.62	110.19	141.34
Pr	95.58	84.67	97.75	99.90	40.22	86.55	45.84	94.82	86.51	105.89
Nd	77.55	64.33	74.07	75.78	34.23	68.16	40.16	75.52	69.57	81.87
Sm	49.85	39.57	45.35	45.60	25.97	43.45	32.05	47.30	46.00	50.25
Eu	44.08	35.95	38.15	40.35	24.46	38.17	30.03	42.61	39.62	42.35
Gd	32.74	26.61	28.80	29.77	19.63	29.24	24.56	31.43	30.80	32.09
Tb	27.37	22.19	22.78	23.75	17.27	23.94	21.87	25.86	26.33	26.39
Dy	22.16	18.42	18.51	19.28	15.02	20.02	19.56	20.89	21.64	21.41
Ho	18.58	15.59	15.47	15.65	12.87	16.52	17.35	17.53	18.41	17.85
Er	15.68	13.07	12.94	12.97	11.23	13.75	15.30	14.73	15.72	14.77
Tm	13.94	11.54	11.34	11.19	9.76	11.82	13.67	12.81	14.25	13.18
Yb	12.37	10.52	10.34	10.12	8.92	11.05	12.20	11.40	12.48	11.79
Lu	11.43	10.07	9.97	9.70	8.88	10.97	12.41	10.91	12.29	11.83
La/Yb	12.27	16.13	19.43	20.46	7.32	13.65	5.96	13.41	11.56	16.94
Dy/Yb	1.79	1.75	1.79	1.91	1.68	1.81	1.60	1.83	1.73	1.82
La/Sm	3.04	4.29	4.43	4.54	2.52	3.47	2.27	3.23	3.14	3.97
Sm/Yb	4.03	3.76	4.39	4.51	2.91	3.93	2.63	4.15	3.68	4.26
Nb/Zr	0.39	0.40	0.38	0.41	0.28	0.43	0.24	0.41	0.43	0.46
Ce/Y	2.78	3.14	3.79	3.88	1.72	2.90	1.43	3.18	2.87	3.60

magnetite (QFM) buffer. The initial magma composition used in the model is found in Table 4. We estimated this starting composition from the major element variation with respect to Mg# (MgO/(FeO + MgO) in mole percent), inferring likely parental compositions to have Mg# of 0.71–0.72, in equilibrium with olivine of Fo_{91-93} composition (Roeder and Emslie, 1970; Putirka, 2005). This parental composition is very similar to that proposed by Thornber (1992) from an average of 8 most primitive lava compositions (Table 4). MELTS models were run with a small amount of water present (<0.5 wt.%). Forward models of the variation in rare earth element (REE) contents during mantle melting were modeled using the MATLAB REEBOX package (Brown and Lesher, 2014) which implements the incremental polybaric non-modal batch melting approach of Fram and Lesher (1993).

3. Results

3.1. Petrography

We examined all samples in thin section. Phenocryst concentration varies from <5% to 20%, but averages ~10%. Samples are dominantly olivine-phyric to microphyric (90% olivine) with subhedral to euhedral olivine (0.1 to 3 mm) in an aphanitic groundmass of fine plagioclase laths and interstitial olivine, pyroxene ± glass. Hexagonal, rounded, and hopper morphologies are common in olivine, and most crystals are at least partially altered to iddingsite. When possible, forsterite content was estimated using 2 V angle, and ranged from Fo_{80} to Fo_{90}. Pyroxenes, mainly augite (0.1 to 1 mm), do not exceed 10% of the total phenocryst population. Plagioclase is typically confined to fine grained laths in the groundmass, but in four samples large (up to 3 mm) plagioclase crystals are present. In these cases the plagioclase crystals are highly sieved with large embayments along the rims, and is likely to be xenocrysts. The majority of plagioclase crystals are too fine to determine anorthite content, but in a few moderately large, twinned crystals we estimated the composition from extinction angles to be An_{45} to An_{70}. Minor opaque minerals, likely spinel (0.25 mm), are ubiquitous at <5%. Several samples are diktytaxitic, and less commonly pilotaxitic. Glomerocrysts of large plagioclase phenocrysts occur in some samples (e.g., HH-4), and are associated with quartz xenocrysts. Nearly all samples exhibit an aphanitic glassy groundmass ranging from slightly vesicular to non-vesicular with the exception of sample HH-11 that is almost entirely crystalline.

Table 3
^{40}Ar–^{39}Ar age determinations for lava flows from Harrat Hutaymah, western Saudi Arabia.

Sample	Total fusion (Ka)	2s error (Ka)	Plateau age (Ka)	2s error (Ka)	N	MSWD	Isochron age (Ka)	2s error (Ka)	MSWD	$^{40}Ar/^{36}Ar$ initial	2s error	Comment
HH-1	246	138	**259**	**120**	16/16	0.51	351	193	0.51	295	1	
HH-3	*2340*	*1070*	*2630*	*590*	16/16	1.46	*2370*	*980*	1.54	296	2	Excess ^{40}Ar
HH-4	*2650*	*580*	*2650*	*940*	16/16	3.12	*1900*	*980*	2.19	300	4	Excess ^{40}Ar
HH-6	857	474	**729**	**266**	12/16	1.22	1009	525	1.29	295	2	
HH-9	471	161	**436**	**97**	14/16	0.69	497	160	0.69	295	1	
HH-10	704	48	**709**	**62**	16/16	2.14	712	131	2.26	296	3	
HH-11	832	39	**844**	**44**	14/16	1.65	785	115	1.64	297	2	
HH-12	581	125	**630**	**82**	33/33	1.30	833	162	1.15	294	1	
176688	436	617	**955**	**545**	13/17	0.23	18	1453	0.08	298	3	
176691	*1140*	*8*	*1085*	*103*	19/31	47.10	**818**	**37**	1.82	340	5	Excess ^{40}Ar
176701a	826	207	**818**	**203**	17/17	0.54	431	290	0.40	298	3	
176701b	*2339*	*25*	*1765*	*255*	31/31	>100	**893**	**44**	1.72	331	1	Excess ^{40}Ar
176710a	*4290*	*480*	*2100*	*910*	8/16	6.16	*1380*	*890*	6.17	297	3	Excess ^{40}Ar
176710b	980	9	**848**	**8**	14/31	0.43	838	25	0.40	302	14	
176712	*8040*	*590*	*4580*	*1750*	11/17	16.58	**550**	**460**	0.40	304	1	Excess ^{40}Ar
176734a	930	114	**868**	**90**	16/17	0.46	703	175	0.16	298	2	
176734b	881	9	**804**	**10**	19/30	1.54	784	19	1.22	307	10	

Ages calculated using sanidine monitor FCs (28.201 Ma) and the total decay constant l = 5.530E − 10/yr. N is the number of heating steps (defining plateau/total); MSWD is an F-statistic that compares the variance within step ages with the variance about the plateau age. Preferred ages are shown in bold; italics indicate sample with suspected mantle-derived (excess) ^{40}Ar.

Table 4
Parental magma for Harrat Hutaymah lavas.

Oxide, element	This paper wt.%, ppm	HPM wt.%, ppm
SiO_2	45.5	45.5
Al_2O_3	13.1	12.6
FeO	10.9	10.8
CaO	9.9	10.0
MgO	13.4	13.9
Na_2O	3.3	3.2
K_2O	1.0	1.0
TiO_2	2.1	2.0
MnO	0.2	0.2
P_2O_5	0.4	0.5
Cr	700	
Ni	500	570
Mg#	0.713	0.721

HPM is an average of 8 most MgO-rich lavas (Thornber, 1992).

3.2. Geochronology

^{40}Ar–^{39}Ar data obtained for 14 samples are summarized in Table 3. Complete data files for all experiments are available as Supplementary Geochronological Data from the journal. Reliable plateau ages for 10 of these range from 260 to 850 Ka. These have corresponding concordant isochron ages with atmospheric $^{40}Ar/^{36}Ar$ intercepts. However, clear evidence for excess ^{40}Ar, probably derived from undetected xenolithic fragments, is seen in the age spectra for several samples (Fig. 3b). For example, the age spectra for samples 176701b and 176691 exhibit "saddle-shape" age spectra in which the middle range of temperature steps (those that are most radiogenic) are least affected by xenolithic outgassing. In these cases, the isochron plots provide consistently younger ages, within the range of the uncomplicated plateau ages, and non-atmospheric $^{40}Ar/^{36}Ar$ intercepts.

In view of the excess ^{40}Ar problem, three samples (176701, 176710 and 176734) were analyzed twice, from separate aliquots. Sample 176701a produced an acceptable plateau (818 ± 203 Ka) without evidence of excess Ar; however, sample 176701b (mentioned above) did show excess Ar, and we prefer the isochron age (893 ± 44 Ka), which is within error of the 176701a plateau age. Sample 176710a showed a disturbed age spectrum, with decreasing and irregular step ages with temperature, from which no credible isochron developed. The second analysis (176710b) produced a saddle-shaped age spectrum with a well-defined middle temperature plateau (848 ± 8 Ka), and a corresponding isochron age of 838 ± 44 Ka. Sample 176734a showed a simple plateau at 868 ± 90 Ka, while the second analysis (176734b) exhibited a small effect from excess Ar but a reliable plateau at 804 ± 10 Ka. These new ages are generally younger than, and considerably less variable than previous K/Ar ages (0.1 to 2.65 Ma, Thornber, 1992; 1.84 ± 0.05 Ma, Pallister, 1984).

3.3. Geochemistry

Major, trace, and rare earth element concentrations for 10 new samples are reported in Tables 1 and 2, respectively, and previously analyzed but unpublished compositions for 49 lavas and tephras from Thornber (1992) are given in the Supplementary Geochemical Data. A total alkalis vs. silica diagram comparing the Harrat Hutaymah lavas with selected other harrats and Red Sea lavas (Fig. 4) demonstrates that the new Harrat Hutaymah data agree well with those from Thornber (1992). Hutaymah lavas exhibit a small range of compositional variation, from basanite to alkali basalt (44 to 49 wt.% SiO_2 and 3.6 to 6.4 wt.% $Na_2O + K_2O$), and trachy-basalt (hawaiite). Mg# is restricted to the range 0.53–0.73 and MgO contents from ~7–14 wt.% MgO, indicating rather primitive, unevolved compositions. This aligns with the petrographic observation of olivine ± clinopyroxene dominated crystallization. The limited compositional range at Hutaymah and the restriction to less evolved compositions is similar to Harrat Lunayyir, which is also located off the MMN line axis (Fig. 1; Duncan and Al-Amri, 2013), whereas lavas from the larger and centrally located harrats (e.g., Rahat, Khaybar) show greater variation and extend to more evolved compositions (Camp et al., 1991; Moufti and Hashad, 2005). Lavas from the Red Sea ocean floor are dominantly more tholeiitic than harrat lavas (Fig. 4; Essien et al., 1989; Kelley et al., 2013).

Bivariate diagrams comparing major oxides and selected trace element and trace element ratios to MgO contents are shown in Figs. 5, 6 and 9. SiO_2, Al_2O_3, Na_2O, TiO_2 and CaO show broadly increasing trends with increasing MgO, consistent with crystal fractionation, although there is also considerable scatter, particularly for Na_2O, TiO_2 and CaO. FeO* contents are also scattered but remain broadly constant with decreasing MgO. Compatible trace elements (e.g., Cr and Ni) follow simpler trends that reflect decreasing concentrations to lower MgO, consistent with significant olivine fractionation. Incompatible elements typically increase with decreasing MgO, although as with major elements these trends show more scatter (Fig. 6). Ratios of similarly incompatible trace elements, e.g., Nb/Zr, Ba/Nb, $[La/Sm]_N$, do not change systematically with MgO (Figs. 6 and 9). Hutaymah lavas show consistent light REE enrichment and heavy REE depletion (Fig. 7). $[La/Yb]_N$ and $[Dy/Yb]_N$ ratios range from 6–29 and 1.6–1.9, respectively.

4. Discussion

4.1. Timing of Hutaymah magmatism

The age of Harrat Hutaymah volcanism has been estimated previously to be 0.1 to 2.7 Ma, employing the conventional K/Ar dating method (Pallister, 1984; Thornber, 1992). While the new ^{40}Ar–^{39}Ar ages reported here fall within this range, our data also suggest that Hutaymah volcanism occurred over a much shorter period, from 260–850 Ka. In one particular example, sample HH-1 was collected at the same location (Al Hutaymah tuff ring, Fig. 2) from which Pallister (1984) reported an age of 1.84 ± 0.05 Ma. But our ^{40}Ar–^{39}Ar laser step heating experiment produced a significantly younger age of 259 ± 120 Ka (Table 3). An additional consideration comes from field measurement of magnetic polarity preserved in the lava flows — all observed polarities were normal, implying that most of Hutaymah volcanic activity is Brunhes age (≤780 Ka). We explain the disparity between older K/Ar ages reported previously and our ^{40}Ar–^{39}Ar ages by undetected fragments of the abundant xenolithic material commonly found in Hutaymah lavas, which carries un-degassed ("excess") ^{40}Ar and results in erroneously old total fusion ages.

Field observation and petrographic analysis of Hutaymah rocks reveal that many contain xenolithic fragments, from dispersed xenocrysts (sieved plagioclase and quartz) to fist-size poly-crystalline nodules (Thornber, 1990, 1992). We believe these fragments of largely crustal material (granitic and dioritic plutons, aged 670–550 Ma, Stoeser and Camp, 1985) to be the cause of disturbed (non-plateau) ^{40}Ar–^{39}Ar age spectra seen for several samples (Table 3 and Fig. 3), and likely responsible for the older previously reported K/Ar ages. Other samples produced clear plateau ages comprising 60% or more of the total gas released, with concordant isochrons and $^{40}Ar/^{36}Ar$ intercepts within analytical uncertainty of the atmospheric value (295.5). Hence the new ages reported here are more reliable than previous K/Ar ages because the significance of xenolithic material can be evaluated from the non-concordance of step ages, and non-atmospheric initial Ar compositions.

The newly dated lava flows were vented from eruptive centers spanning the full geographic extent of Harrat Hutyamah. The ages do not suggest any consistency in overall time-space variation of volcanism throughout the area. The youngest lava flow measured, in the wall of the Al Hutaymah tuff ring (HH-1, 260 Ka), is post-dated by that eruptive event. Somewhat younger lava flows in the area of Al Qufayl (Fig. 2) are reported by Thornber (1992) as "less than 100 ka", based on an

unpublished K/Ar age. Some of the oldest lava flows (e.g. 176710, 848 Ka; 176734, 868 Ka) were erupted from isolated monogenetic vents and others (HH-11, 844 Ka) post-date earlier tuff-ring explosions (Thornber, 1992). Hence, while our sampling has not fully bracketed the volcanic history, the coverage and consistency of age determinations most likely indicates that Hutaymah volcanism was confined to late Quaternary (Brunhes magnetic chron) time.

4.2. Magmatic evolution

Harrat Hutaymah lavas show important variations in their chemical composition (Figs. 4–7). There are a number of possible sources for this variability and we investigate them below. Forward modeling of the liquid line of descent for a representative Hutaymah primary magma (Table 4) suggests that much of the variability evident in major element abundances relates to polybaric crystal fractionation over a range of upper mantle and crustal pressures. Note that this approach does not imply that all erupted magmas derive from fractionation of the same primary magma batch, but does suggest that the compositions of erupted magmas can be broadly explained by a similar set of primary magma compositions and fractionation processes. We also recognize that complications from magma mixing and contamination by antecrystic phases can also obscure liquid lines of descent (e.g. Kent et al., 2002; Thomson and Maclennan, 2013). Nevertheless the observed variations in composition are broadly consistent with our petrographic observations and observed chemical variations, suggesting that forward modeling of crystal fractionation is a reasonable means to interpret chemical variations in these lavas. The earliest stages of crystal

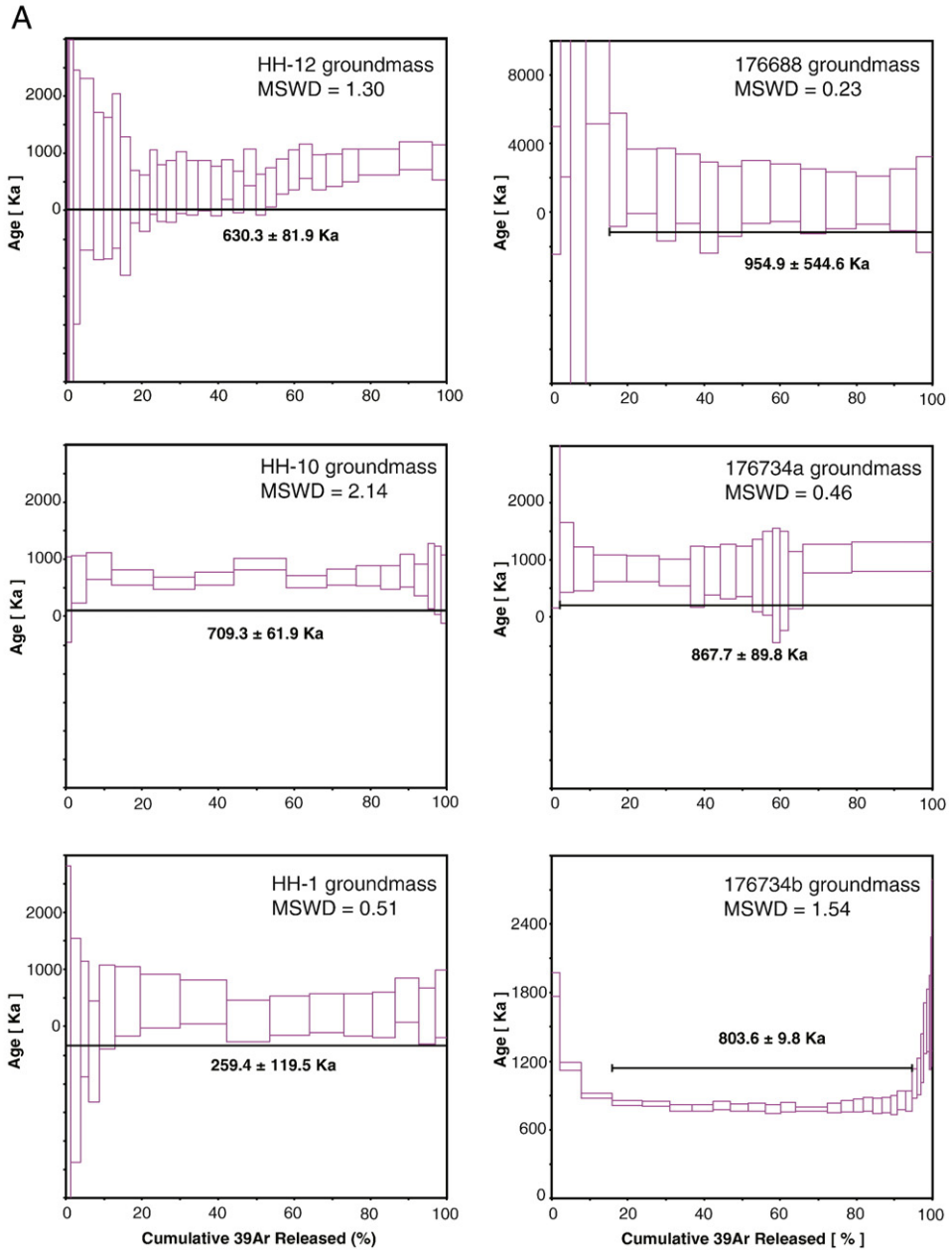

Fig. 3. New ^{40}Ar–^{39}Ar age spectra and isochron plots for Hutaymah lava flows. In age spectra individual step ages are shown as open red boxes whose heights are ±2s plotted against cumulative ^{39}Ar released (%). Solid horizontal black bar indicates step ages used to calculate weighted mean plateau age. MSWD is the mean square of weighted deviations. The isochrons plot $^{40}Ar/^{36}Ar$ vs $^{39}Ar/^{36}Ar$. The step compositions used in the isochron plots are shown as green circles; not used are blue squares; total fusion composition is the red circle. The red line indicates best fitting linear regression, whose slope yields the isochron age.

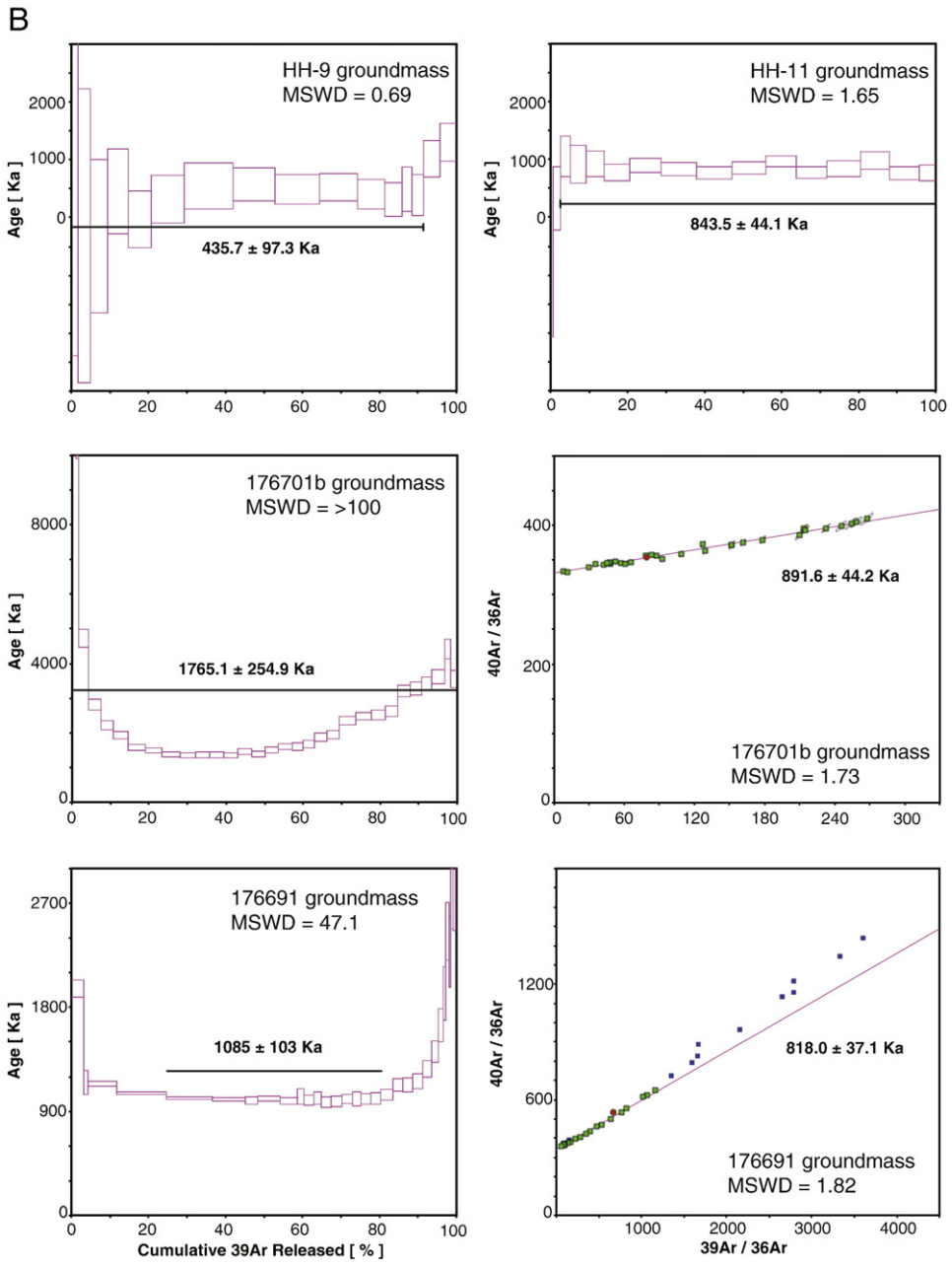

Fig. 3 (*continued*).

fractionation are largely dominated by olivine, as evident from deceasing Ni and Cr with MgO, and this is also consistent with the widespread presence of olivine as a phenocryst phase. Clinopyroxene is also evident as a groundmass and minor euhedral phenocryst phase, and low CaO contents (Fig. 5) and CaO/Al_2O_3 in some lava compositions provide evidence for clinopyroxene fractionation at lower MgO contents. The onset of clinopyroxene crystallization is a function of pressure, and occurs earlier in the liquid line of descent at higher pressures. Thus indications of clinopyroxene removal provide a means to constrain the pressure(s) of crystal fractionation. Hutaymah lavas exhibit a range of CaO contents at a given MgO, with shifts to lower CaO occurring in lavas with MgO contents as high as ~12 wt.% (Fig. 5). As a result Hutaymah lava compositions appear consistent with some clinopyroxene fractionation occurring at pressures in excess of 1 GPa and continuing to pressures as low as 100 MPa. The observed variations in CaO (and Na_2O, Al_2O_3 and FeO) in Hutaymah lavas can thus be broadly explained by olivine and clinopyroxene fractionation occurring over a range of pressures equivalent to the uppermost mantle through to intra-crustal depths. In some cases magma must have been transported relatively rapidly from deep within the crust or mantle to the surface. Deep magma residence and fractionation followed by rapid ascent is also necessary for survival of the lithospheric and deep crustal xenoliths that are abundant in many Hutaymah lavas (e.g. Thornber, 1992).

In spite of forming from magmas that have traversed thick continental lithosphere, and transported a range of crustal and upper mantle xenoliths (Thornber, 1992; Coleman, 1993), Harrat Hutaymah lavas show little evidence for compositional modification via crustal assimilation. This is evident in isotopic compositions, which fall in a narrow, unradiogenic range ($^{87}Sr/^{86}Sr$: 0.70339–0.70349; $^{143}Nd/^{144}Nd$: 0.51286, or ε_{Nd} ~4.2; Altherr et al., 1990; Thornber, 1992), compared with shield crustal

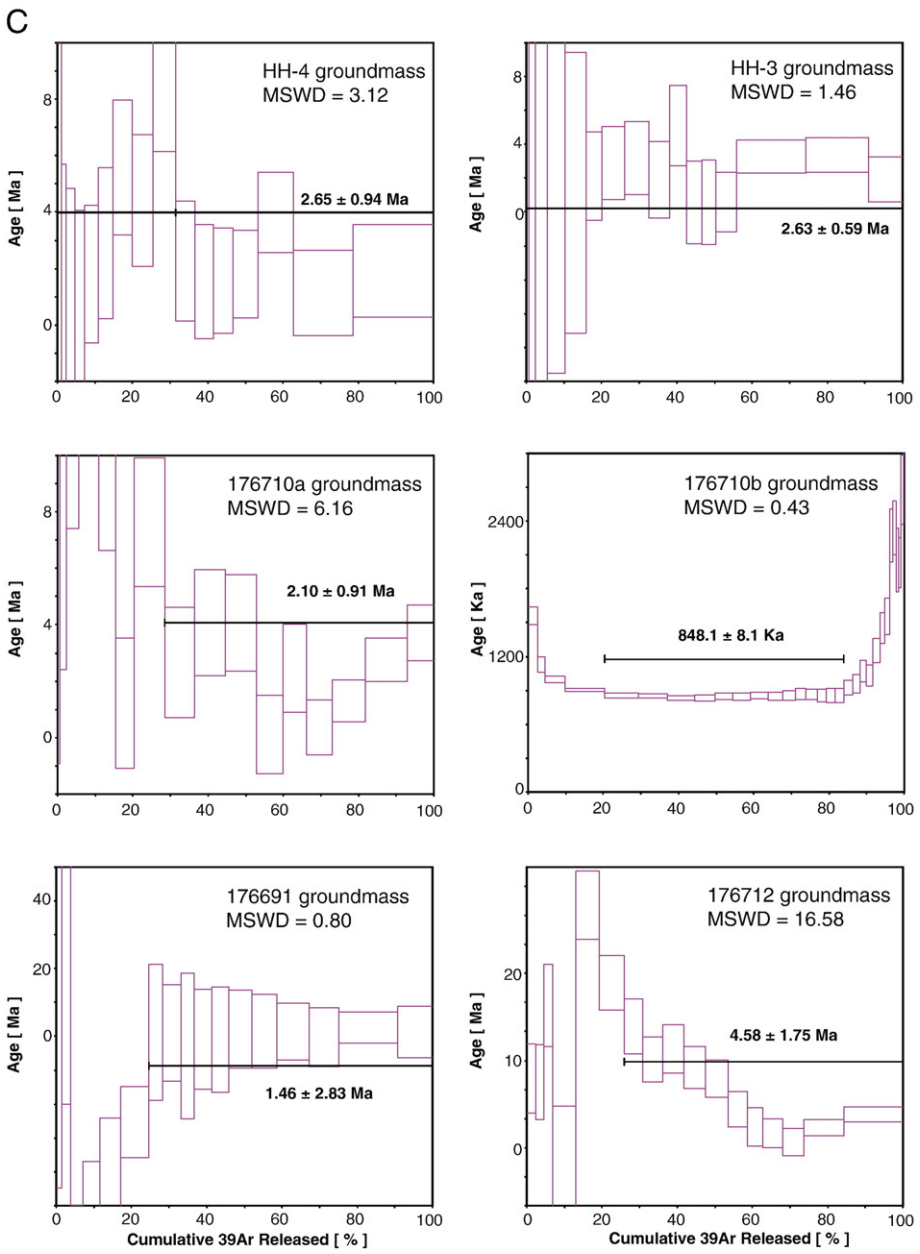

Fig. 3 (*continued*).

rocks (ε_{Nd} ~1; $^{87}Sr/^{86}Sr$ ~0.706). In part this is due to the intrinsically high incompatible element abundances in many of these magmas, although the effects of crustal contamination remain surprisingly minor. For example trace element ratios such as Ba/Nb and K/Nb that are sensitive to crustal assimilation (and would remain unfractionated by fractional crystallization) remain low and do not increase with decreasing MgO contents (e.g. Figs. 6 and 9). Potassium contents and K/Nb in Hutaymah lavas range between 500–1500 μg/g and 80–200 relative to crustal values of 28,000 and 500–2000 (average upper crust compositions; e.g. Baker et al., 1996; Kent et al., 2002). Calculated trends for assimilation-fractional crystallization trends (AFC) for K contents and K/Nb ratios (Fig. 9) show that significant assimilation during progressive crystal fractionation would rapidly increase K and K/Nb, and thus the compositions of Hutaymah lavas are consistent with assimilation occurring only at ratios of mass of material assimilated to that crystallized (r) ≪ 0.1. Incompatible element abundances are also modified during crystal fractionation, however the variations evident in incompatible element contents are larger than can be explained by fractional crystallization or crustal assimilation alone, and likely also reflect variation in the degree of partial melting and/or mantle source composition.

Ultramafic nodules brought to the surface in lavas and tephras provide a detailed sampling of the composition, mineralogy and thermal history of the subcontinental lithosphere beneath Harrat Hutaymah (Thornber, 1992). Thornber (1990) divided these xenoliths into Cr-diopside and Al-augite lithologies, which were further divided into 26 rock types based on mineralogy and texture. The Al-augite lithologies are believed to have been entrained from ±10 km of the crust-mantle boundary (about 40 km depth in this region, Healey et al., 1982), while the Cr-diopside nodules come from depths up to 70 km, based on two-pyroxene thermometric estimates (Wells, 1977). Both groups include anhydrous and hydrous examples. The Nd-isotopic compositions of the metamorphic mantle xenoliths define a pseudo-isochron

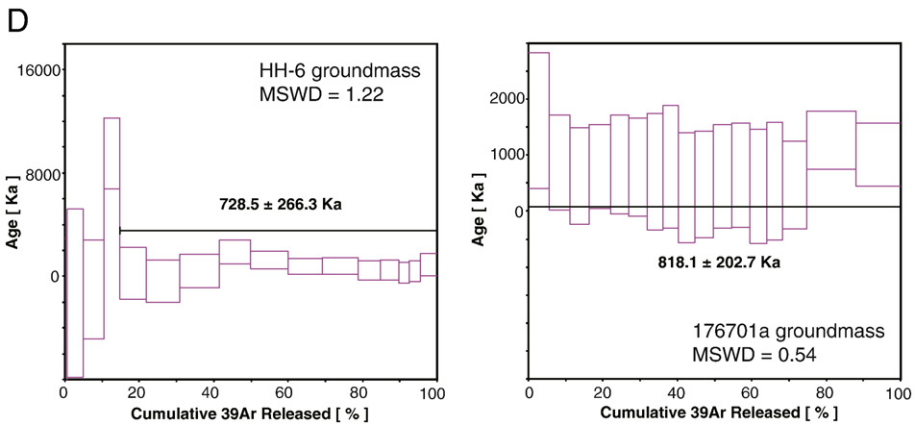

Fig. 3 (*continued*).

of ~700 Ma, consistent with the Proterozoic age of crustal shield rocks and xenoliths from other nearby harrats (Stoeser and Camp, 1985; Krienitz and Haase, 2011). The deeper-sourced, high temperature pyroxenites and partial melt-bearing peridotites have Sr- and Nd-isotopic compositions that match the narrow range of Hutaymah lava compositions, which led Thornber (1992) to propose that they formed contemporaneously with the Quaternary volcanic activity (i.e., synrift), as residual mantle from partial melting or through melt-wall rock interaction. The latter admits the possibility that melts formed somewhat deeper (asthenosphere) and reacted with the deep lithosphere in transit to the surface.

4.3. Constraints on mantle source composition and melting

Variations in REEs and other trace elements can be used to constrain the mantle source composition and melting conditions involved in magma generation. Overall, as noted above, the considerable range of incompatible element abundances at a given MgO content (Fig. 6) suggests that crystal fractionation and assimilation is unlikely to be the sole source of incompatible element variations, and differences in the degree of melting and/or mantle source composition have also exerted important controls on trace element abundance.

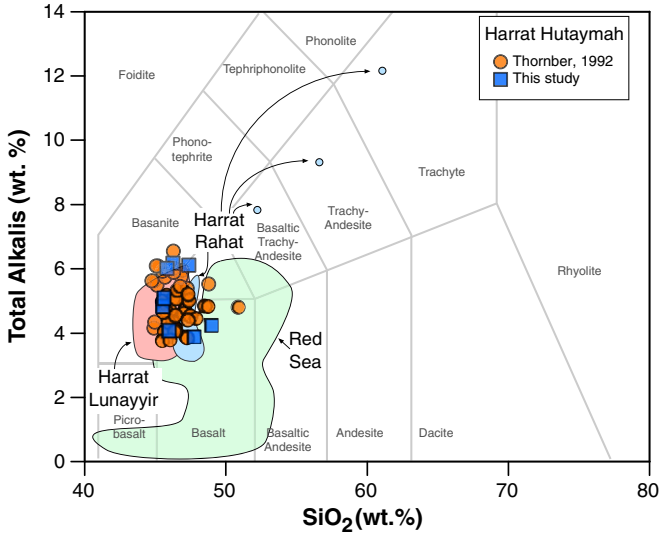

Fig. 4. Total alkalis vs. silica diagram comparing harrat province fields and Red Sea lavas. Harrat Hutaymah lavas are red circles (Thornber, 1992) and blue squares (this study). Fields representing data for Harrat Lunayyir (Duncan and Al-Amri, 2013), Harrat Rahat (Moufti and Hashad, 2005), and Red Sea lavas (Vlastelic et al., 1998; Kelley et al., 2013) are also shown.

Mantle melting in intraplate settings is strongly affected by the solidus pressure, melt productivity and pressure at which melting ceases, the latter controlled by the thickness of the overlying cold lithospheric "lid" (e.g. McKenzie and O'Nions, 1991; Fram and Lesher, 1993). Examination of REE patterns (Fig. 7) shows that all Hutaymah magmas are strongly enriched in LREE ($[La/Sm]_N$ ~ 2–4.5), and have ratios of MREE to HREE (e.g. $[Sm/Yb]_N$ ~ 2.5–4.5) consistent with some melting occurring at sufficient depth to be in equilibrium with residual garnet. These REE features, as well as the enriched Sr and Nd isotope compositions of Hutaymah and other harrat magmas (Altherr et al., 1990) are also consistent with melting of an enriched mantle composition. Simple batch melting calculations support this and suggest that the broad REE characteristics of Hutaymah lavas could be produced by melting of garnet lherzolite with a primitive mantle composition source.

To constrain melting conditions further we have used the approach of Fram and Lesher (1993) and Brown and Lesher (2014) to calculate forward models of REE contents produced under different melting conditions. Duncan and Al-Amri (2013) applied this approach to magmas from Harrat Lunayyir, farther to the west, and we now extend this treatment to Hutaymah. Calculations herein use the MATLAB script "REEBOX" (Brown and Lesher, 2014). We use a primitive mantle source composition in order to reproduce the highest $[La/Sm]_N$ values that we observe at Hutaymah, as it was not possible to produce these values using a depleted MORB source mantle. The REEBOX approach is based on forward modeling of non-modal incremental batch melting in an upwelling mantle melting column (Fram and Lesher, 1993). The compositions of pooled incremental polybaric non-modal batch melts produced by melting along the extent of an entire upwelling melting column can be compared to observed compositions to constrain the pressure at which melting started and ceased, and to estimate the degree of melting.

We use partition coefficients for REE from McKenzie and O'Nions (1991). Melt productivity is set at 1.0% per 0.1 GPa. Results appear in Fig. 8, where the compositions of aggregated melts are shown. We also show the pressures of the beginning and ending of melting and equivalent melt fraction (see figure caption). These results suggest that melting beneath Hutaymah started at pressures of ~2.5–2.6 GPa and continued up to pressures of 1.8–2.5 GPa, consistent with a lithospheric thickness of 60–80 km. Earlier authors (e.g. Camp and Roobol, 1992; Duncan and Al-Amri, 2013) have argued that melting beneath harrats that lie away from the center of the MMN line occurred under thicker lithosphere, and our results are consistent with this. Melting underneath Harrat Lunayyir, another volcanic field peripheral to the MMN line (Fig. 1) started at 2.2–2.4 GPa and continued until ~1.4–2.1 GPa, equivalent to a lithospheric thickness of ~45–70 km. Melting beneath

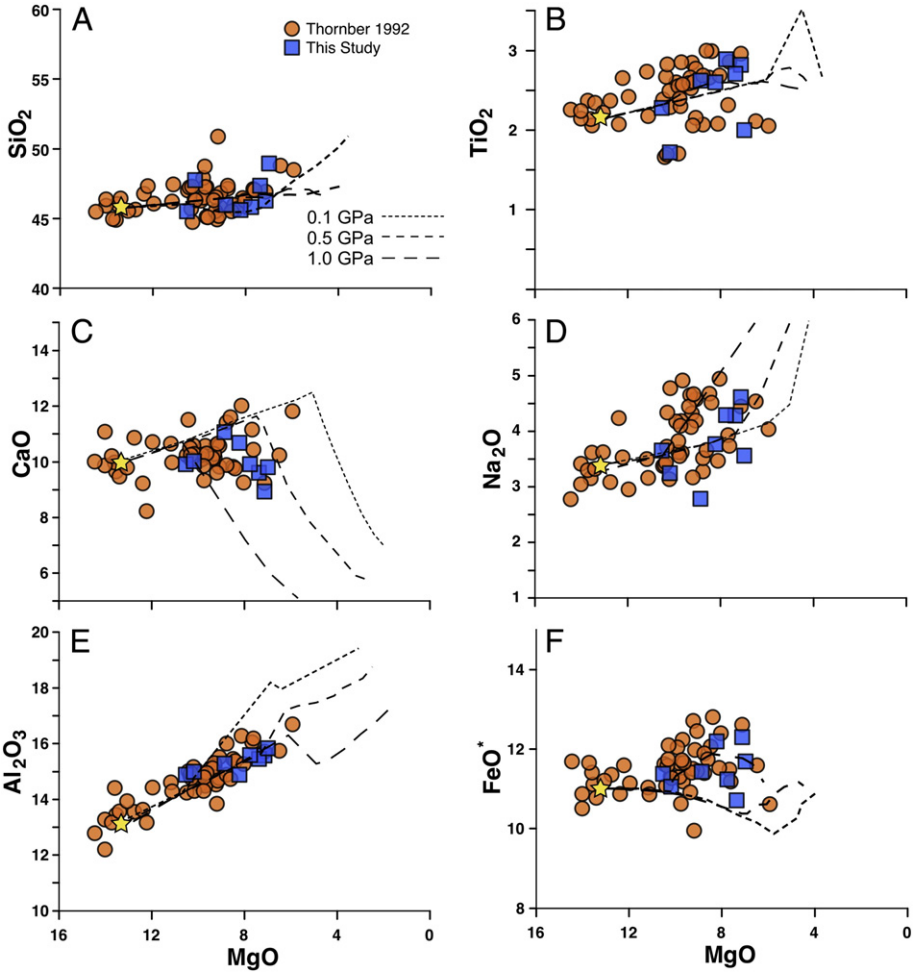

Fig. 5. Variations in selected major element oxides vs. MgO in Harrat Hutaymah samples from Thornber (1992) and this study. Also shown are calculated liquid lines of descent for fractional crystallization of a representative primary liquid (see Table 4) determined using MELTS (Ghiorso and Sack, 1995). Oxidation conditions were set at the QFM buffer and calculations used an initial primary magma that contained 0.2 wt.% H_2O.

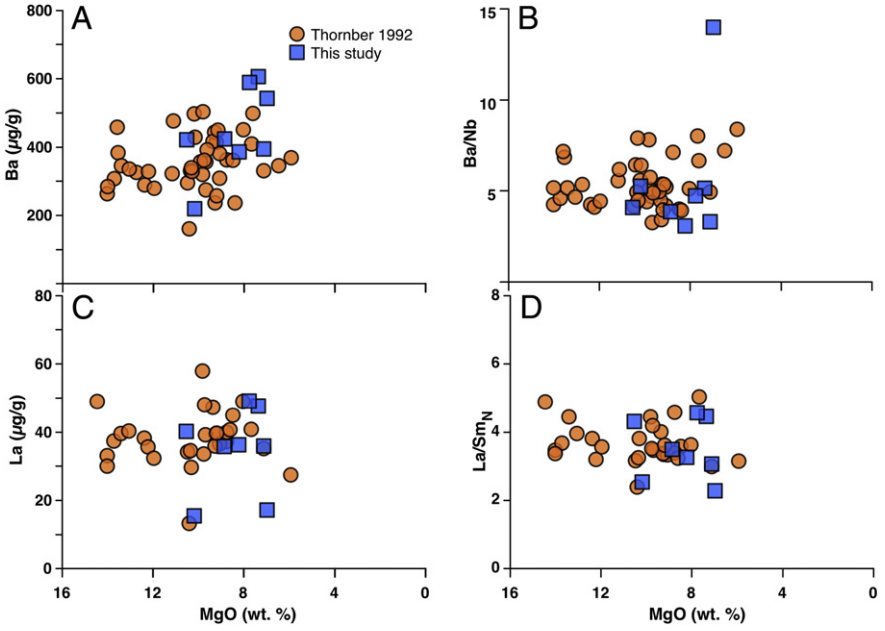

Fig. 6. MgO vs. (A) Ba, (B) Ba/Nb, (C) La, (D) $[La/Sm]_N$, (E) Ni and (F) Cr for Harrat Hutaymah lavas from Thornber (1992) and this study.

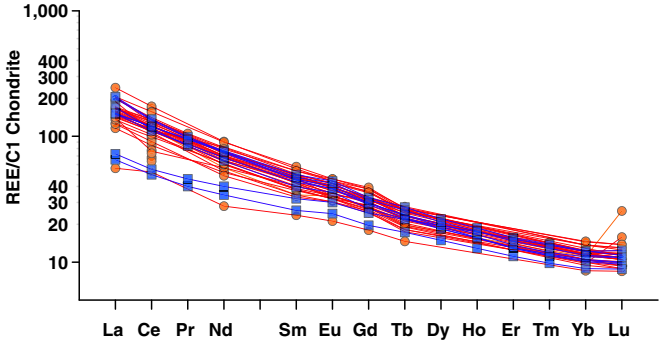

Fig. 7. Chondrite normalized REE profiles for samples from Thornber (1992) and this study. Normalized using compositions from McDonough and Sun (1989). Symbols as for Fig. 4.

Harrat Rahat, which is central to the MMN line started at 2.4–2.8 GPa, but continued until 1.2–1.6 GPa, equivalent to a lithospheric thickness of only 40–50 km. The degree of melting also varies between these three harrats, with the Hutaymah having values that range from ~1–7%, Lunayyir ~2–10% and Rahat 11–15%.

Lava flow compositions from the Red Sea have distinctly lower $[La/Sm]_N$ and $[Dy/Yb]_N$ ratios and less radiogenic isotopic compositions relative to harrat lavas, suggesting that overall they derive from greater degrees of melting at shallower depths, and form from a more depleted mantle source (e.g. Altherr et al., 1990; Camp and Roobol, 1992). The forward model calculations we show in Fig. 8 cannot be directly applied to Red Sea lavas as we use a Primitive Mantle source that is likely to be more enriched than the depleted mantle MORB source for Red Sea lavas (Altherr et al., 1990). Preliminary modeling using a MORB source depleted mantle suggests lithospheric thicknesses of ≪10 km for Red Sea lavas, consistent with typical models for MORB formation from

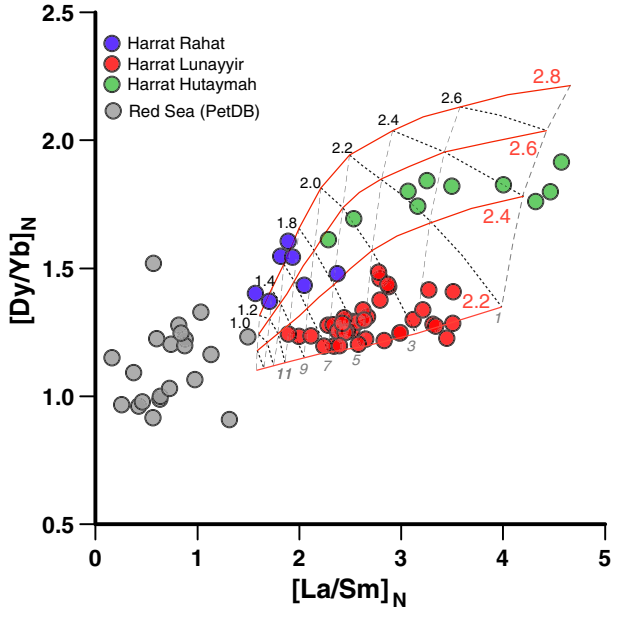

Fig. 8. $[La/Sm]_N$ vs $[Dy/Yb]_N$ for lavas from Harrat Hutaymah, Harrat Lunayyir, Harrat Rahat and from the Red Sea. Data from Thornber (1992), this study, Duncan and Al-Amri (2013), and Moufti and Hashad (2005). Red Sea lava data are from PETDB. Lines show the result of REEBOX modeling (Fram and Lesher, 1993; Brown and Lesher, 2014). Solid red lines and red numerals show solidus pressure, black short dashed lines and black numerals show the pressure of cessation of melting (equivalent thickness of the lithospheric "lid"), and fine gray long dashed lines and grey numerals show the melt fraction as percent. Pressures are in GPa. Modeling uses a primitive mantle starting composition and partition coefficients from McKenzie and O'Nions (1991). Polybaric melt productivity is 1% per 0.1 GPa. See text for more details.

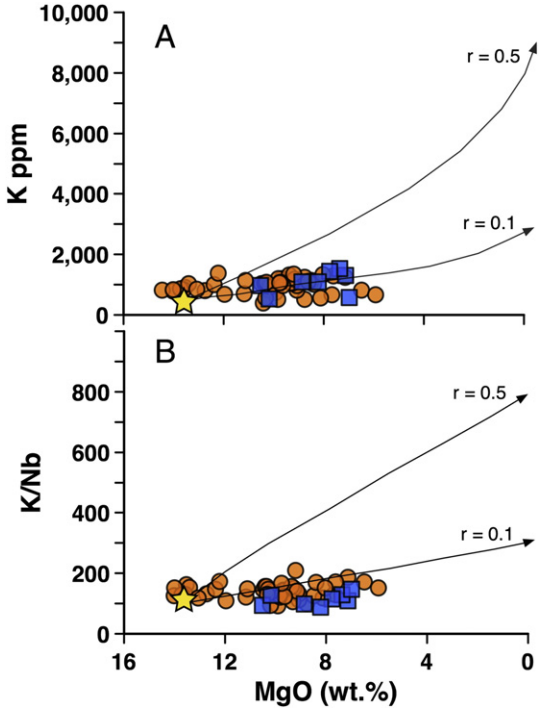

Fig. 9. K and K/Nb vs. MgO content. Data are shown for samples from this study and from Thornber (1992) (see caption for Fig. 6 for legend). Lines show calculated assimilation-fractional crystallization (AFC) trends for ratios of mass assimilated to mass crystallized (r) of 0.1 and 0.5. The assimilant is modeled after average upper continental crust (see Baker et al., 1996; Kent et al., 2002) and contains 28,220 μg/g K, 14 μg/g Nb and 2.5 wt.% MgO.

shallow melting with little or no lithosphere present. This is also consistent with the findings of Duncan and Al-Amri (2013).

It is also interesting to note that MELTS models do not adequately describe the observed changes in TiO_2 contents as a function of clinopyroxene fractionation. This is also consistent with the observation that TiO_2 contents do not correlate strongly with other moderately incompatible major elements or with CaO. Instead the highest correlation coefficients are observed between TiO_2 and the middle REE, suggesting that initial TiO_2 contents are variable and strongly influenced by the same variations in mantle source and melting that control REEs.

4.4. Evidence for mantle plume influence

Several factors indicate that the harrat magmatic province is not simply the result of passive mantle upwelling and melting in response to regional extension associated with Africa–Arabia plate separation, now focused at the Red Sea spreading ridge. First, the uplift, erosion and extent of volcanic activity are not symmetric across the extending region. Secondly, the subcontinental lithosphere beneath the Arabian shield has been variably thinned. While lithosphere thins rapidly near the eastern margin of the Red Sea (Healey et al., 1982), there is anomalously thin lithosphere (inferred from seismic and geochemical data) beneath the N–S Makkah–Madinah–Nafud (MMN) line also associated with the largest volcanic fields (see above; also Mooney et al., 1985; Gettings et al., 1986; Julia et al., 2003). These observations point to active mantle flow that provides thermal buoyancy for lithospheric uplift, and possible thermal erosion of the asthenosphere-lithosphere boundary beneath focused regions of the Arabian shield.

Active upwelling is proposed by Camp and Roobol (1992) and Krienitz et al. (2009), who suggest that radial flow of upper mantle material from the Afar mantle plume may have influenced the tectonics and distribution of volcanism in the region. Additional information about upper mantle flow comes from seismic anisotropy studies

(Hansen et al., 2006, 2007). Chang and van der Lee (2011) report jointly inverted teleseismic S- and SKS-arrival times, regional S- and Rayleigh waveform fits, fundamental-mode Rayleigh wave-group velocities, and independent Moho constraints that provide complementary resolution for the three-dimensional (3-D) S-velocity structure beneath the region. Specifically, Chang and van der Lee (2011) find distinct low-velocity anomalies in the uppermost mantle, along with shear-wave splitting results that indicate horizontal mantle flow radially from Afar. This radial flow seems to be organized in channels, potentially following thin lithosphere. One such channel follows the Gulf of Aden, supporting the notion of eastward-directed mantle flow from Afar. Another channel extends northward beneath the southern Red Sea, but rather than following the NW-trending Red Sea spreading axis, it continues northwards beneath western Saudi Arabia, aligned with the MMN line.

Trace element and isotopic data are consistent with the origin of harrat magmas from partial melting of enriched (plume-influenced) mantle, rather than depleted mantle, which is the source for Red Sea basalts (e.g. Altherr et al., 1990; Fitton et al., 1997). Recent study of the He-isotopic composition of Hutaymah xenoliths and lavas (Konrad et al., 2016) finds a remarkable uniformity in xenolith $^3He/^4He$ ratios, with a weighted mean of 7.55 ± 0.03 R_A (2σ, n = 18), across eight different xenolith types. A somewhat lower value, 6.8 ± 0.1 R_A was measured in the least altered (high temperature, anhydrous) spinel lherzolite. Olivine from non-xenolith bearing lavas falls within the range of xenolith compositions. From these results and complementary CO_2 and trace element data (Konrad et al., 2016) it appears that the subcontinental lithosphere beneath the harrats region has been altered by fluid-rich partial melts from the asthenosphere, which slightly raised the $^3He/^4He$ composition from ~6.8 to 7.5 R_A. However, if the asthenosphere was influenced by mantle flow from the Afar region, the He signature was largely degassed before melting beneath Hutaymah. In contrast, Murcia et al. (2013) find more elevated $^3He/^4He$ values (9.3 to 11.7 R_A) in historic lava flows at Harrat Rahat. This much larger volcanic field sits along the MMN line, directly above the geophysically-imaged thinned lithosphere, and may reflect more vigorous asthenospheric flow.

4.5. Harrat Hutaymah petrogenesis and regional implications

The data obtained over the course of this research challenges previous models for the petrogenesis of Harrat Hutaymah and the harrat region as a whole. New $^{40}Ar–^{39}Ar$ ages ranging from 260 to 850 Ka suggest that Harrat Hutaymah formed more rapidly and recently than previously thought. Also, samples analyzed in this research, as well as those studied from Harrat Lunayyir and Harrat Rahat, are consistent with formation from a plume-influenced source (Fitton et al., 1997). It has been proposed that the petrogenesis of Harrat Hutaymah and the entire harrat region can be explained by simple decompression melting related to the rifting of the Red Sea (Hempton, 1987; Coleman and McGuire, 1988; Thornber, 1992). However, the variability of depth and degree of melting, differences in timing among harrats, as well as the significant compositional variation observed throughout the province, suggest that the situation is more complex.

The model we propose explains the petrogenesis of Harrat Hutaymah and the rest of the harrat region with regional extension resulting in decompression melting coupled with northward asthenospheric flow from the Afar plume (Fig. 10). It is likely that the older, Red Sea parallel, volcanic fields (>12 Ma) are the result of simple decompression melting due to rifting of the Red Sea, as suggested by their orientation and tholeiitic compositions. However, the younger (<12 Ma) N–S oriented volcanic fields (Hutaymah, Lunayyir, Rahat, etc.) that together make up the Makkah–Madinah–Nafud (MMN) line are best explained by regional lithospheric thinning, possibly in concert with thermal erosion, coupled with northward flow of asthenospheric material likely derived from the Afar plume. Investigation of some of the larger, longer-lived volcanic fields (e.g., Rahat, Khaybar) should reveal the timing of changes in the lithosphere–asthenosphere boundary.

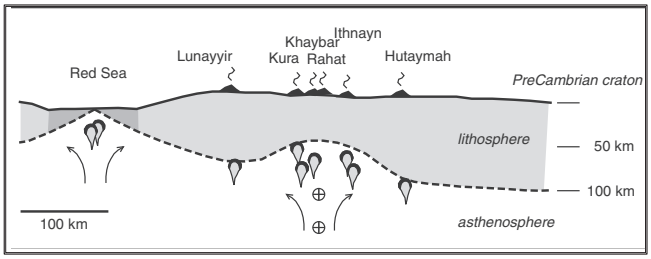

Fig. 10. Schematic cross-section of Harrat province petrogenesis. Regional thinning of Arabian craton leads to decompression melting at the base of the continental lithosphere. Additional thinning along the N–S trending MMN line may result from channelized northward asthenospheric flow from the Afar region, bringing warmer and more plume-like material. The coupled effect explains the variable depth and degree of melting and the compositional variation observed across the region.

Acknowledgments

Kyle Krawl provided assistance with instruction in using the geochemical modeling software. ICP-MS and additional XRF analyses were provided by the Washington State University GeoAnalytical Laboratory. Dr. Dan Miggins assisted with $^{40}Ar–^{39}Ar$ incremental heating analyses. We thank Dr. Saeed Alshaltoni for assistance with sample collection and thin section preparation. R.A.D. acknowledges support from the Distinguished Scientist Fellowship Program at King Saud University. Chip Lesher provided access to the REEBOX package. Parts of this research were supported by the King Abdulaziz City for Science and Technology (KACST) and the National Science Foundation (award 1524675).

Appendix A. Supplementary data

Supplementary data to this article can be found online at http://dx.doi.org/10.1016/j.jvolgeores.2016.01.010.

References

Altherr, R., Henjes-Kunst, F., Baumann, A., 1990. Asthenosphere versus lithosphere as possible sources for basaltic magmas erupted during formation of the Red Sea: constraints from Sr, Pb and Nd isotopes. Earth Planet. Sci. Lett. 96, 269–286.
Baedecker, P.A., McKown, D.M., 1987. Instrumental neutron activation analysis of geochemical samples. U.S. Geol. Surv. Bull. 1770 (16 pp.).
Baker, J.A., Thirwall, M.F., Menzies, M., 1996. Sr–Nd–Pb iso-topic and trace element evidence for crustal contamination of plume-derived flood basalts: Oligocene flood volcanism in western Yemen. Geochim. Cosmochim. Acta 60, 2559–2581.
Bohannon, R.G., Naeser, C.W., Schmidt, D.L., Zimmerman, R.A., 1989. The timing of uplift, volcanism, and rifting peripheral to the Red Sea—a case for passive rifting? J. Geophys. Res. 94, 1683–1701.
Bramkamp, R.A., Ramirez, L.F., Brown, G.F., and Pocock, A.E., 1963. Geology of the Wadi Ar Rimah Quadrangle, Kingdom of Saudi Arabia. U.S. Geological Survey Miscellaneous Investigations Map I-206A, scale 1:500,000.
Brown, E.L., Lesher, C.E., 2014. North Atlantic magmatism controlled by temperature, mantle composition and buoyancy. Nat. Geosci. http://dx.doi.org/10.1038/ngeo2264.
Camp, V.E., Roobol, M.J., 1992. Upwelling asthenosphere beneath western Arabia and its regional implications. J. Geophys. Res. 90, 15,255–15,271.
Camp, V.E., Roobol, M.J., Hooper, P.R., 1991. The Arabian continental alkali basalt province: part II. Evolution of Harrats Khaybar, Ithnayn, and Kura, Kingdom of Saudi Arabia. Geol. Soc. Am. Bull. 103, 363–391.
Chang, S., van der Lee, S., 2011. Mantle plumes and associated flow beneath Arabia and East Africa. Earth Planet. Sci. Lett. 302, 448–454.
Coleman, R.G., 1993. Geologic Evolution of the Red Sea. Oxford Monographs on Geology and Geophysics. Oxford University Press, p. 186.
Coleman, R.G., McGuire, A.V., 1988. Magma systems related to the Red Sea opening. Tectonophysics 150, 77–100.
Duncan, R.A., Al-Amri, A.M., 2013. Timing and composition of volcanic activity at Harrat Lunayyir, western Saudi Arabia. J. Volcanol. Geotherm. Res. 260, 103–116.
Essien, J.-P., Juteau, T., Joron, J.-J., Dupre, B., Humler, E., Al'Mukhamedov, A., 1989. Petrology and geochemistry of basalts from the Red Sea axial rift at 18°N. J. Petrol. 30, 791–839.

Fitton, J.G., Saunders, A.D., Norry, M.J., Hardarson, B.S., Taylor, R.N., 1997. Thermal and chemical structure of the Iceland plume. Earth Planet. Sci. Lett. 153, 197–208.
Fram, M.S., Lesher, C.E., 1993. Geochemical constraints on mantle melting during creation of the North Atlantic basin. Nature 363, 712–715.
Gettings, M.E., Blank, H.R., Mooney, W.D., Healey, J.H., 1986. Crustal structure of southwestern Saudi Arabia. J. Geophys. Res. 91, 6491–6512.
Ghiorso, M.S., Sack, R.O., 1995. Chemical mass transfer in magmatic processes IV. A revised and internally consistent thermodynamic model for the interpolation and extrapolation of liquid–solid equilibria in magmatic systems at elevated temperatures and pressures. Contrib. Mineral. Petrol. *119* (2–3), 197–212.
Hansen, S.E., Rodgers, A., Schwarz, S., Al-Amri, A.M., 2007. Imaging ruptured lithosphere beneath the Red Sea and Arabian peninsula. Earth Planet. Sci. Lett. 259, 256–265.
Hansen, S.E., Schwarz, S., Al-Amri, A.M., Rodgers, A., 2006. Combined plate motion and density driven flow in asthenosphere beneath Saudi Arabia: evidence from shear-wave splitting and seismic anisotropy. Geology 34, 869–872.
Healey, J.H., Mooney, W.D., Blank, H.R., Gettings, M.E., Kohler, W.M., Lamson, R.J., Leone, L.E., 1982. Saudi Arabian Seismic Deep-Refraction Profile: Final Project Report. Ministry of Petroleum and Mineral Resources, Deputy Ministry for Mineral Resources, Kingdom of Saudi Arabia (Open File Report USGS-OF-02-37, 141 pp.).
Hempton, M.R., 1987. Constraints on Arabian plate motion and extensional history of the Red Sea. Tectonics 6, 687–705.
Johnson, D.M., Hooper, P.R., Conrey, R.M., 1999. XRF analysis of rocks and minerals for major and trace elements on a single low dilution Li-tetraborate fused bead. Adv. X-ray Anal. 41, 843–867.
Julia, J., Ammon, C., Hermann, R., 2003. Lithosphere structure of the Arabian Shield from joint inversion of receiver functions and surface-wave group velocities. Tectonophysics 371, 1–21.
Kelley, K.A., Kingsley, R.H., Schilling, J.G., 2013. Composition of plume-influenced mid-ocean ridge lavas and glasses from the Mid-Atlantic Ridge, East Pacific Rise, Galapagos Spreading Center, and Gulf of Aden. Geochem. Geophys. Geosyst. 14, 223–242.
Kent, A.J.R., Baker, J.A., Wiedenbeck, M., 2002. A melt inclusion-based study of crustal contamination and melt column aggregation in continental flood basalts from Yemen. Earth Planet. Sci. Lett. 202, 577–594.
Knaack, C., Cornelius, S.B., Hooper, P.R., 1994. Trace element analyses of rocks and minerals by ICP-MS. Technical Notes. GeoAnalytical Lab, Washington State University.
Konrad, K., Graham, D.W., Thornber, C.R., Duncan, R.A., Kent, A.J.R., Al-Amri, A., 2016. Asthenosphere-lithosphere interactions in Western Saudi Arabia: Inferences from $^{3}He/^{4}He$ in xenoliths and lava flows from Harrat Hutaymah. Lithos http://dx.doi.org/10.1016/j.lithos.2016.01.031.
Koppers, A.A.P., 2002. ArArCALC — software for Ar-40/Ar-39 age calculations. Comput. Geosci. 28 (5), 605–619.
Krienitz, M.-S., Haase, K.M., 2011. The evolution of the Arabian lower crust and lithospheric mantle—geochemical constraints from southern Syrian mafic and ultramafic xenoliths. Chem. Geol. 280, 271–283.
Krienitz, M.S., Haase, K.M., Mezger, K., van den Bogaard, P., Thiemann, V., Shaikh-Mashail, M.A., 2009. Tectonic events, continental intraplate volcanism, and mantle plume activity in northern Arabia: constraints from geochemistry and Ar–Ar dating of Syrian lavas. Geochem. Geophys. Geosyst. 10. http://dx.doi.org/10.1029/2008GC002254.
Kuiper, K.F., Deino, A., Hilgen, F.J., Krijgsman, W., Renne, P.R., Wijbrans, J.R., 2008. Synchronizing rock clocks of earth history. Science 320, 500–504.
McDonough, W.F., Sun, S.S., 1989. Chemical and isotopic systematics of ocean basalts: implications for mantle composition and processes. Geol. Soc. Lond. Spec. Publ. 42, 313–345.
McKenzie, D., O'Nions, R.K., 1991. Partial melt distributions from inversion of rare earth element concentrations. J. Petrol. 32, 1021–1091.
Mooney, W.D., Gettings, M.E., Blank, H.R., Healey, J.W., 1985. Saudi Arabian seismic deep refraction profile: travel-time interpretation of crust and upper mantle structure. Tectonophysics 111, 173–246.
Moufti, M.R., Moghazi, A.M., Ali, K.A., 2012. $^{40}Ar/^{39}Ar$ geochronology of the Neogene–Quaternary Harrat Al-Madinah intercontinental volcanic field, Saudi Arabia: implication for duration and migration of volcanic activity. J. Asian Earth Sci. 62, 253–268.
Moufti, M.R.H., Hashad, M.H., 2005. Volcanic hazards assessment of Saudi Arabian Harrats: geochemical and isotopic studies of selected areas of active Makkah–Madinah–Nafud (MMN) volcanic rocks. Final Report (LGP-5-27). King Abdulaziz City for Science and Technology, Riyadh, Saudi Arabia.
Murcia, H., Lindsay, J.M., Niedermann, S., Cronin, S.J., Smith, I.E.M., El-Masry, N.N., Moufti, M.R.H., Nemeth, K., 2013. The potential use of cosmogenic nuclides for dating in Harrat Rahat. Vorisa Scientific Meeting, pp. 24–28.
Pallister, J.S., 1984. Reconnaissance Geology of the Harrat Hutaymah Quadrangle, Sheet 26/42 A, Kingdom of Saudi Arabia: Ministry of Petroleum and Mineral Resources, Deputy Ministry for Mineral Resources, Jeddah, Kingdom of Saudi Arabia, Open-File Report USGS-OF_04-46 (77 pp.).
Pallister, J.S., 1987. Magmatic history of Red Sea rifting: perspective from the central Saudi Arabian coastal plain. Geol. Soc. Am. Bull. 98, 400–417.
Putirka, K., 2005. Mantle potential temperatures at Hawaii, Iceland, and the mid-ocean ridge system, as inferred from olivine phenocrysts: evidence for thermally-driven mantle plumes. Geochem. Geophys. Geosyst. http://dx.doi.org/10.1029/005GC000915.
Roeder, P.L., Emslie, R.F., 1970. Olivine-liquid equilibrium. Contrib. Mineral. Petrol. 29, 275–289.
Stoeser, D.B., Camp, V.E., 1985. Pan African microplate accretion of the Arabian shield. Geol. Soc. Am. Bull. 96, 817–826.
Thomson, A., Maclennan, J., 2013. The distribution of olivine compositions in Icelandic basalts and picrites. J. Petrol. 54, 745–768.
Thornber, C.R., 1992. The Petrology, Geochemistry, and Origin of Ultramafic Inclusions and Mafic Alkaline Volcanics from Harrat Hutaymah, Saudi Arabia (Doctoral Dissertation) University of Colorado.
Thornber, Carl R., 1990. Geologic map of Harrat Hutaymah, Saudi Arabia, with the petrologic classification and distribution of ultramafic inclusions (1:100,000 scale), USGS Miscellaneous Field Studies Map MF-2129.
Vlastelic, I., Dosso, L., Guillou, H., Bougault, H., Geli, L., Etoubleau, J., Joron, J.L., 1998. Geochemistry of the Hollister Ridge: relation with the Louisville Hotspot and the Pacific–Antarctic Ridge. Earth Planet. Sci. Lett. 160, 777–793.
Wells, P.R.A., 1977. Pyroxene thermometry in simple and complex systems. Contrib. Mineral. Petrol. 62, 129–139.